Received 13 April 2023; revised 24 July 2023; accepted 29 August 2023. Date of publication 15 September 2023; date of current version 6 October 2023.

Digital Object Identifier 10.1109/OJAP.2023.3310975

Ultra-Wideband Tightly Coupled Dipole Array Fed by a Tapering Meandered Balun

MATTHEW W. NICHOLS (Member, IEEE), MICHAIL O. ANASTASIADIS (Graduate Student Member, IEEE), MALCOLM E. TAAFFE (Member, IEEE), ELIAS A. ALWAN (Member, IEEE), AND JOHN L. VOLAKIS (Life Fellow, IEEE)

College of Engineering & Computing, Florida International University, Miami, FL 33174, USA

CORRESPONDING AUTHOR: M. W. NICHOLS (e-mail: mnich036@fiu.edu)

This work was supported in part by the Air Force Office of Scientific Research under Grant FA9550-19-0290 and Grant FA9550-18-1-0191; in part by Northrop Grumman under Grant PO 5300022936; and in part by NASA under Grant 80NSSC18K1736.

ABSTRACT An ultra-wideband (UWB) phased array is presented operating from UHF to C-bands (0.14 to 5.85 GHz). This new design employs an integrated, compact tapered spline balun in conjunction with a triple-layer semi-resistive frequency selective surface (FSS) network. Notably, the integration of the meandered balun within a dual-polarized tightly-coupled dipole array (TCDA) allowed for a contiguous bandwidth of 40:1 with VSWR < 2.5 at broadside. Moreover, the use of the semi-resistive FSS superstrate enabled scanning down to $\pm 60°$ with a VSWR < 3.5 in the E-, H-, and D-planes. The overall array thickness is $\lambda_{Low}/17.93$ (where λ_{Low} is the wavelength at the lowest frequency of operation, 140 MHz), and the array's radiation efficiency is 75% on average across the operational bandwidth. That is, compared to previous UWB TCDAs with contiguous operational bandwidths of 40:1 or greater, the proposed array is 30% thinner and has equally good or better efficiency. This paper presents the analysis and design of the dipole array, with emphasis on the spline balun. An 8×8 prototype (12×12 element FSS network footprint) was fabricated and measured to validate the performance of a finite array.

INDEX TERMS Tightly coupled dipole array (TCDA), ultra-wideband (UWB) array, phased array, frequency selective surface (FSS) network.

I. INTRODUCTION

As IS well known, the wireless spectrum is highly fragmented and congested [1], implying challenges in its utilization. Notably, over the short span of a couple months in 2015, the Federal Communications Commission (FCC) auctioned just 65 MHz (a bandwidth smaller than that used for WiFi) for more than $40 billion [2]. This high value of the microwave spectrum is only increasing as user demand continues to increase, with the global mobile market data rates growing by approximately 30% every year [2].

Furthermore, communication platforms (i.e., cell phones, GPS, vehicles, satellites) require access to many different, often widely separated bands. This creates inefficient and costly redundancy, as independent systems are required for each frequency band. UWB antennas and arrays can enable multi-functionality, and replace the multiple narrowband apertures to achieve significant reduction in power, cost, and space [3]. Specifically, UWB arrays perform well in radio astronomy [4], and can realize secure communications using spread spectrum techniques [5]. They also enable advanced remote sensors, including foliage penetration (FOPEN) [6], through-wall imaging [7], medical imaging [8], and high resolution radar [9].

However, UWB phased arrays are often impaired by trade-offs in scanning capability, size, efficiency, and bandwidth [10]. Vivaldi or tapered slot arrays are among early UWB apertures, first implemented in the 1970s [11]. These arrays use a tapered slot line to perform matching to free space. However, while achieving UWB operational bandwidth, they are multiple wavelengths tall and have high cross-polarization levels when scanning, including phase center instability [12], [13]. A Vivaldi variation, the sliced notch antenna (SNA), corrects the unbalanced current potentials known to cause high cross-polarized gain, but is still multiple wavelengths tall [14]. Another Vivaldi variation, the balanced antipodal Vivaldi antenna (BAVA), achieves a

© 2023 The Authors. This work is licensed under a Creative Commons Attribution 4.0 License. For more information, see https://creativecommons.org/licenses/by/4.0/

low profile of $\lambda_{High/2}$ (where λ_{High} is the wavelength at the highest frequency of operation), with a decade bandwidth via capacitive coupling between elements, but is limited to 45° scanning [15]. The planar UWB modular antenna (PUMA) utilizes coupled dipole array elements with unbalanced feeding, but only operates over a 6:1 impedance bandwidth [16]. Transverse electromagnetic (TEM) horns [17], body-of-revolution (BOR) elements [18], and bunny-ear arrays [19] have also shown impressive bandwidth performance but are non-planar in nature. Hence, they often lead to large and protrusive structures that are challenging to fabricate, especially for low-frequency applications.

A recent class of UWB arrays is the tightly coupled dipole arrays (TCDA) [20], [21]. A key advantage of TCDAs is their practical feed structure while conforming to stringent space, weight, and cost constraints. Notably, TCDAs require balanced feeding, implying that the dipole currents must be equal and opposite. Therefore, a feed structure that provides a smooth transition across the entire operational bandwidth from a balanced (dipole) to an unbalanced (coaxial cable) interface must be employed. A balun can provide the unbalanced to balanced current transformation along with impedance matching from 50Ω to almost 200Ω. Of course, the balun's physical presence should not degrade the array's performance (i.e., gain, pattern, bandwidth, cross-pol) or add substantial increase in the array's weight and cost. Further, the balun must fit inside a limited volume for a low-profile array configuration [20], [21].

Past TCDAs have achieved wide bandwidths from 300 MHZ to 90 GHz, as detailed in [21]. TCDAs build on Wheeler's ideal current sheet array (CSA) concept [22], and achieve optimal bandwidth based on the Bode-Fano limits [23], [24], [25], [26], [27], [28]. Several papers have shown impressive bandwidth, as seen in [29], [30], [31], [32]. Notably, previous TCDA designs have used FSS layers to increase bandwidth, improve scanning, suppress substrate resonances, and reduce the apertures thickness. However, efficiency is often reduced as bandwidth is increased [33], [34], [35], [36], [37], [38]. Most recently, TCDA designs have achieved extremely wide bandwidths, with improved efficiency, using layered FSS networks below the array plane [39], [40], [41].

In this paper, we focus on the enhancement of TCDA UWB performance, building upon the designs seen in [39], and [40]. Notably, a triple-layer semi-resistive FSS network is employed to shift and then attenuate ground plane resonances. In addition, it effectively provides variable ground plane distance control with higher average efficiency. A novel integrated compact tapered spline balun is employed to accommodate impedance matching over the entire bandwidth while maintaining smaller conformal array thickness. The presented array is dual-polarized and operates from 140 MHz to 5.85 GHz with a VSWR $<$ 2.5 at broadside. Moreover, the antenna exhibits low angle scanning capabilities with VSWR$<$3 (over most of the band) down to 60°, in the E-, H-, and D-planes. Its profile thickness is only

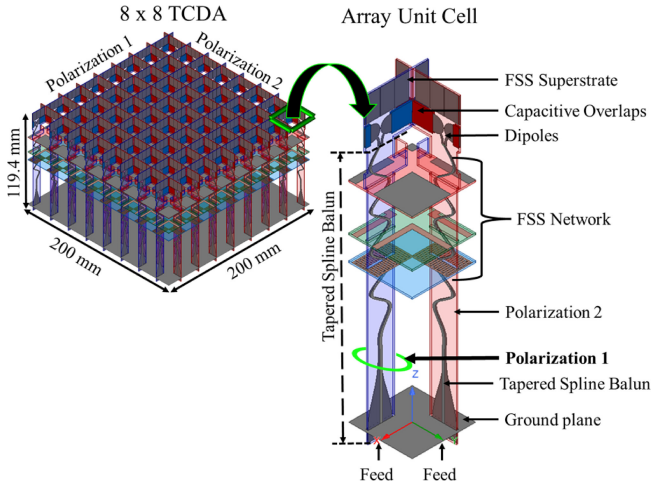

FIGURE 1. 3D view of the 8 × 8 array and periodic unit cell.

$\lambda_{Low}/17.93$ (where λ_{Low} is the wavelength at the lowest frequency of operation, 140 MHz).

An average radiation efficiency of approximately 75% is achieved across this operational bandwidth. The array and integrated balun consist of three copper layers hosted by two Rogers 4003 substrates of 0.305 mm thickness each. Correspondingly, the semi-resistive FSS network is printed on Rogers 3010 material (layer 1), and FR4 (layers 2 & 3), all 0.64 mm thick. An 8 × 8 prototype of the array (12 × 12 element FSS footprint) was fabricated to verify simulations.

The paper is organized as follows. Section II introduces the array with its structure and parameters. Sections III and IV highlight the design of the tapered spline balun and the triple-layer semi-resistive FSS network, respectively. Section V discusses the fabrication and assembly of the prototype, with simulation and measurements presented in Section VI.

II. ARRAY AND FSS SUPERSTATE DESIGN

The proposed 8 × 8 dual polarized TCDA (see Fig. 1) is constructed by assembling orthogonal rows of 8 × 1 element linearly polarized boards to form an 'egg-create' configuration and inserting them vertically against the ground plane. Each row consists of three copper layers hosted by two Rogers 4003 substrates of 0.305 mm thickness each (ε_r = 3.55, tanδ = 0.0027). To assemble the entire array, partial slots are cut at the edge of each dipole element in a 8 × 1 row to form the 'egg-create' configuration. Notably, no direct electrical connection or soldering is required, making fabrication simple and low-cost.

The final geometrical parameters are provided in Table 1. These parameters were generated by creating a model of the periodic array (i.e., a periodic unit cell) using Ansys High Frequency Structure Simulator (HFSS). The periodic unit cell is composed of the following (from top to bottom): 1) a single layer printed FSS superstrate layer [32], 2) tightly coupled dipoles and capacitive overlapping pads, 3) tapered spline balun and triple-layer semi-resistive FSS network (both discussed later), and 4) the ground plane (see

TABLE 1. Design parameter values of the final array unit cell.

Parameter	Dimension	Parameter	Dimension
W_1	18 mm	T_1	2 mm
W_2	19 mm	T_2	0.56 mm
W_3	15 mm	T_3	0.25 mm
W_4	25 mm	T_4	0.1 mm
W_5	20 mm	T_5	1.25 mm
W_6	10 mm	T_6	0.3 mm
W_7	6 mm	T_7	10.3 mm
W_8	12 mm	T_8	10 mm
W_9	7.25 mm	T_9	1 mm
W_{10}	8.8 mm	h_1	119.4 mm
W_{11}	5.5 mm	h_2	105 mm
W_{12}	0.65 mm	h_3	99.75 mm
W_{13}	0.7 mm	h_4	75 mm
W_{14}	105 mm	h_5	65 mm
S_1	0.7 mm	h_6	55 mm
S_2	0.6 mm	B_1	4
S_3	1.37 mm	B_2	0.3 mm
		B_3	14 mm
		B_4	7.3 mm

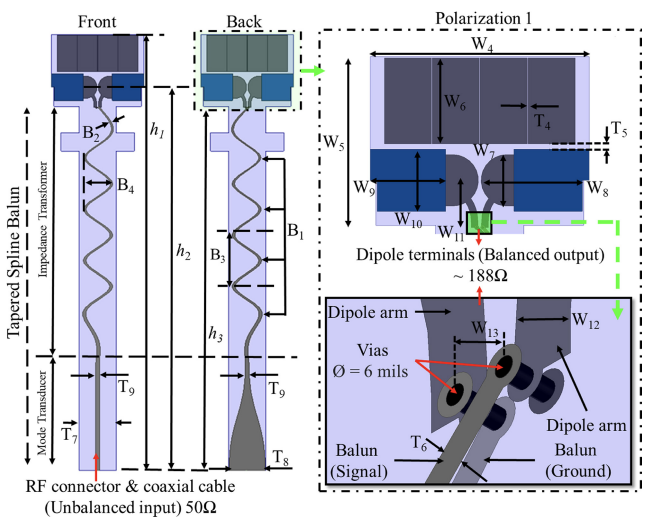

FIGURE 2. Periodic unit cell design features and parameters comprising polarization 1. Design features and parameters comprising polarization 2 are a mirror copy of polarization 1, with the exception of the partial slot cut at the edge of each dipole element. Design parameter values are given in Table 1.

Fig. 1). Referring to Fig. 2, the various design features and parameters comprising polarization 1 are listed. Design features and parameters comprising polarization 2 are a mirror copy of polarization 1, with the exception of the partial slot cut at the edge of each dipole for assembling the 'egg-create' structure. A stack diagram of the layers forming the periodic unit cell comprising polarization 1 are shown in Fig. 3.

The FSS superstrate and dipole arms reside in the center copper layer. The superstrate is designed to improve the impedance matching between the dipoles and free-space for wider scanning capability [32]. Notably, the printed metallic

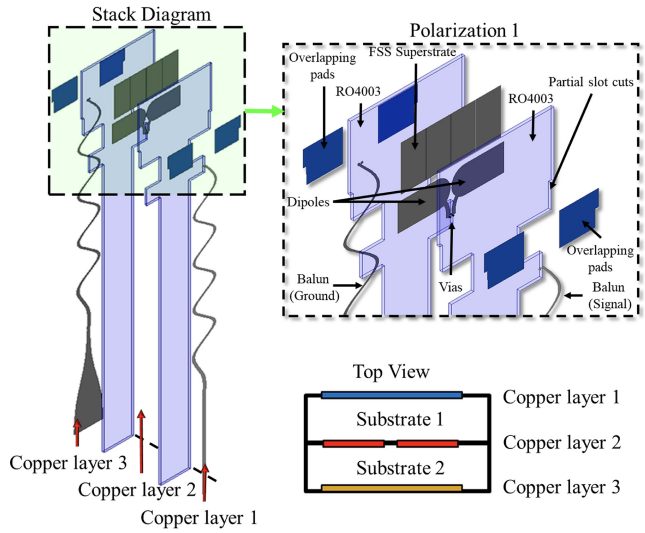

FIGURE 3. Stack diagram of the periodic unit cell (polarization 1).

FSS superstrate replaces previously used large, heavy, and expensive dielectric slab superstrates (see [29], [35], [36]). Using the periodic unit cell layout shown in Fig. 1, the width, height and spacing of the superstrate layer was optimized. As expected, wider and taller superstate layers achieve better performance at lower frequencies and vice versa. A trade-off was therefore required between good performance and the array thickness at the lower end of the operational band. Also, to avoid grating lobes, the dipoles are designed to keep the distance between adjacent elements less than $\lambda_{High}/2$. To do so, overlapping pads are placed on each of the outer copper layers (in effect emulating overlapping dipoles). This approach induces strong capacitive coupling among the dipole elements, extending the operational bandwidth [22], [30]. The feed balun traces are also placed on the outermost copper layers (see next section).

III. TAPERED SPLINE BALUN

To develop the proposed 42:1 wideband array aperture, we employed a correspondingly wideband feed consisting of a tapered spline balun, as in Fig. 4. This balun was first simulated as an individual structure with a 188Ω impedance termination, and then optimized in a periodic setting. Individually, it shows an impedance match of largely $S_{11} < -10$ dB with an average transmission loss (S_{21}) of only 0.64 dB over an operational bandwidth of 57:1 (134 MHz to 7.65 GHz), as depicted in Fig. 5. Specifically, the presented balun optimizes the transition between a mode transducer and an impedance transformer to achieve minimum reflection, and cancel common-mode currents (i.e., combining balun functionality with impedance transformation). Parametric studies found that if the transductive section is too long, the impedance transformer does not operate effectively. If too short, the resultant abrupt transition to the unbalanced excitation leads to a differential mode excitation. To that end, we adopted a Klopfenstein taper profile [42],

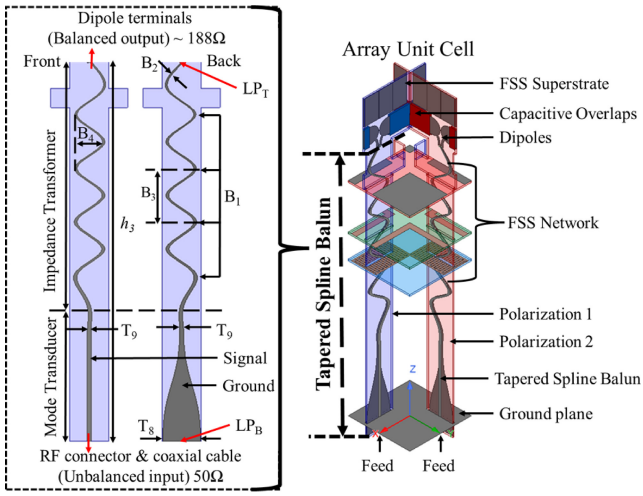

FIGURE 4. Compact tapered spline balun: 3D views with design features and parameters labeled. As labeled, 'LP_T' refers to the approximately 188Ω lumped port (port 2), and 'LP_B' refers to the 50Ω lumped port excitation (port 1) used in simulations. Other labeled design parameters are given in Table 1.

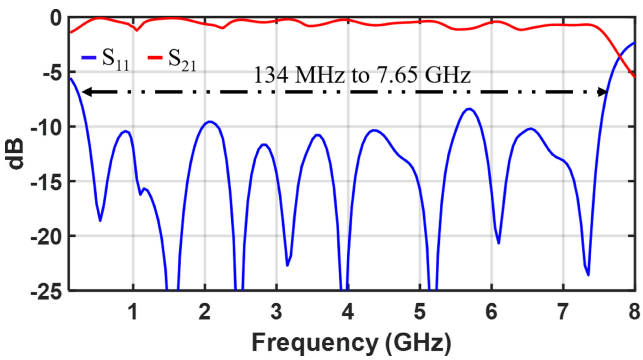

FIGURE 5. Compact tapered spline balun: simulated reflection (S_{11}) and transmission (S_{21}) results for port to port performance of the balun.

[43] to design the mode transducer section of the balun. This taper was implemented using a set of cubic Bézier curve approximations [44] given by:

$$P_{TC} = P_1(1-t)^3 + 3P_2(1-t)^2 t + 3P_3(1-t)t^2 + P_4 t^3 \quad (1)$$

In the above, P_1 to P_4 are four control points representing the Klopfenstein taper profile, and P_{TC} refers to the coordinates of the curve with t representing the displacement along the curve.

The connected impedance matching section of the balun consists of tapered meandering twin lines [45] that were approximated using spline curves [46], [47]. The goal is to achieve optimal impedance matching from an unbalanced 50Ω line to a pair of balanced outputs at the dipoles (impedance at the dipoles is approximately 188Ω). For our case, fifteen control points were used to achieve the desired features of the balun. These include the number of curves (B_1), ratio (steps) of the balun's taper (B_2), as well as the length (B_3) and width (B_4) of each curve within the balun, see Fig. 2 and Fig. 4. Notably, the final balun taper design consisted of seven different widths: 1 mm (at the bottom) to 0.3 mm (at the top). Indeed, designing the balun with polynomials allowed for curve control through a manageable number of control points (transforming the control points transforms the curve in the same way). These optimized control points made the design more manageable for electromagnetic (EM) simulations.

It should be noted that common-modes may be introduced in the substrate during scanning. For our case, these common-mode resonances can be suppressed by the FSS network and its resistive loading (discussed in the next section). It is also remarked that the twin lines are minimally offset only at the very top of the balun to allow connection to the dipoles for both polarizations: the spacing of this offset allowed for through vias to be inserted, reducing cost and fabrication complexity by avoiding buried or blind vias.

IV. FSS NETWORK DESIGN

To achieve the proposed 42:1 array band, a triple-layer semi-resistive FSS network is inserted between the array and ground planes. The configuration is shown in Fig. 6. From top down, layer 1 of the FSS network is printed on Rogers 3010 ($\varepsilon_r = 10.2$, $\tan\delta = 0.0035$), with layers 2 & 3 printed on FR4 material ($\varepsilon_r = 4.4$, $\tan\delta = 0.02$). Each layer measures 292 mm × 292 mm × 0.64 mm. The array's ground plane is also realized on FR4 material, and measures 292 mm × 292 mm × 0.64 mm.

The inserted FSS network layers located between the array and ground planes serve to emulate a variable array height (with ground plane distance control), and shift/attenuate in-band resonances. In effect, the FSS network introduces a phase delay to artificially increase the electrical profile of the array. Resonances occur periodically due to ground plane effects, at ground plane heights $\lambda/2$ (where λ is the wavelength at the operational frequency), and per common-modes seen during scanning [29]. Specifically, the top FSS layer (layer 1) behaves as a reflector above 2.3 GHz. At frequencies lower than 2.3 GHz, it is more or less transparent (i.e., layer 1 acts as a low-pass filter with a cut-off at 2.3 GHz). Notably, the location of layer 1 must be designed such that the reflected and directed wavefronts add coherently for frequencies above $f_0 = 2.3$ GHz. Reflected waves appearing with a ±180° phase shift destructively cancel the upward directed radiating wave, resulting in poor radiation efficiencies. For frequencies above 2.3 GHz, radiated waves are reflected with a phase of $\phi_{rlp}(f)$ upon seeing layer 1 (equal to π). Adding the distance traveled, $2d$, and the free space wavenumber ($k_0 = \frac{2\pi}{\lambda}$, where λ is the wavelength at the operational frequency), the total phase delay gain upon reaching the array plane can be written as:

$$\Delta\phi_1 = 2k_0 d + \phi_{rlp}(f) \quad (2)$$

To further describe the response of layer 1, we note for frequencies below 2.3 GHz the propagating wave will travel through layer 1, see Fig. 7, picking up a transmission phase

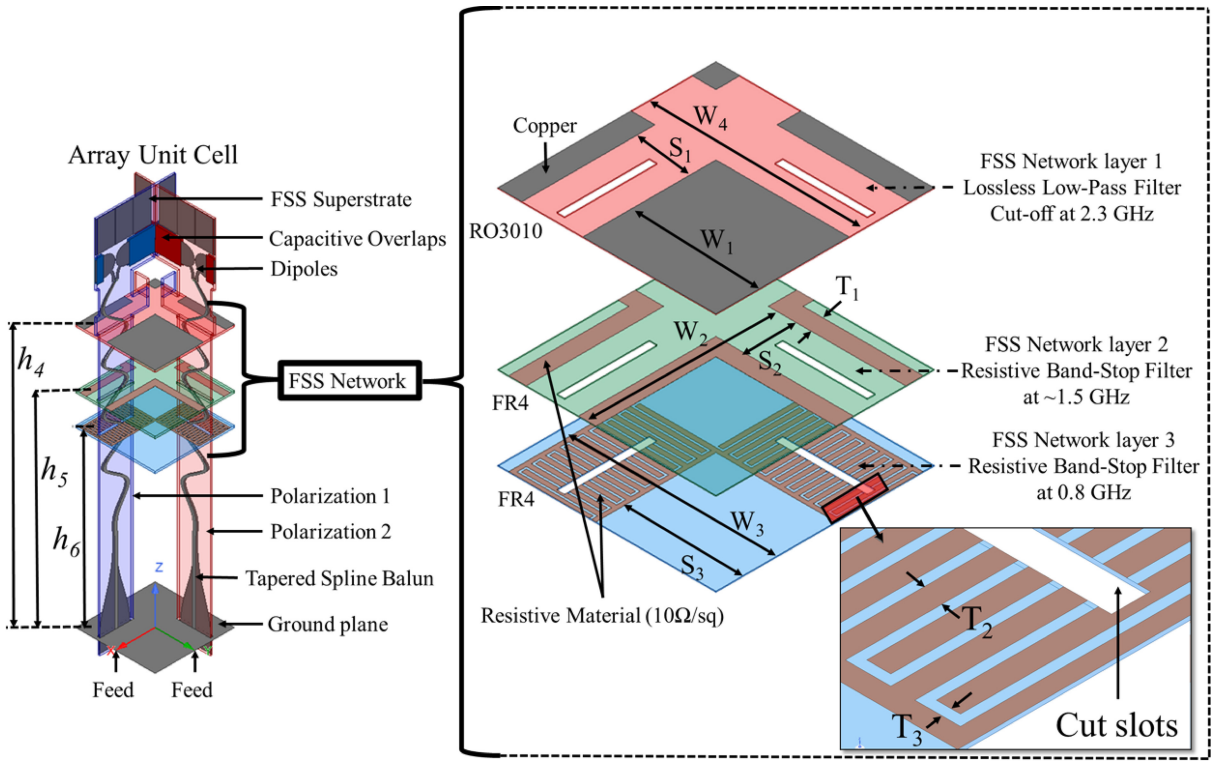

FIGURE 6. Periodic array unit cell with a zoomed view of the triple-layer FSS network, and labeled features and parameters. Design parameter values are given in Table 1.

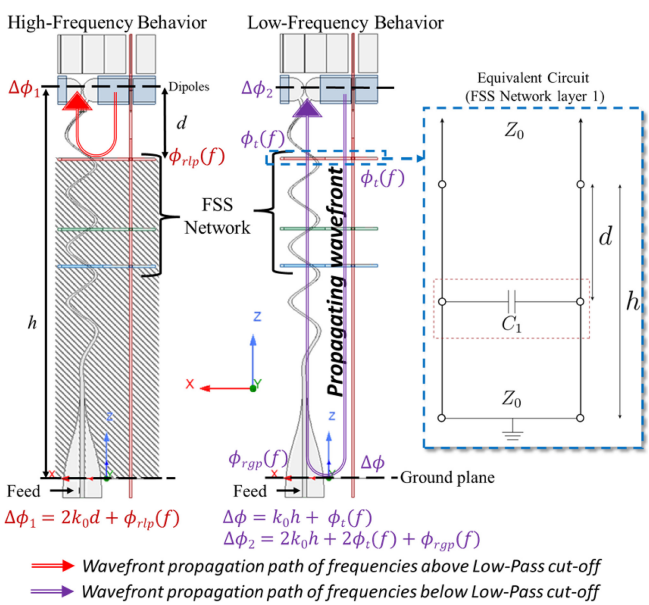

FIGURE 7. Illustration of the phase distribution in the dipole plane of an array unit cell.

value of:

$$\phi_t(f) = \tan^{-1}\left(C_1\phi_{rpl}Z_0f\right) = -\tan^{-1}\left(\frac{f}{f_0}\right) \tag{3}$$

Here, C_1 is the equivalent capacitance of layer 1, $\phi_{rlp}(f) = \pi$, and Z_0 denotes free-space characteristic impedance. It is observed that the transmission phase, $\phi_t(f)$, varies between 0 and $\frac{\pi}{4}$. This implies that resonances are shifted to the lower band [40]. Upon acquiring the transmission phase, $\phi_t(f)$, from layer 1, the wave is reflected at the ground plane, and acquires a reflection phase of $\phi_{rgp}(f)$, equal π. Subsequently, as the wave passes again through layer 1 in the opposite direction, a second transmission phase, $\phi_t(f)$, is added. The overall phase as the wave travels from the array plane, to the ground plane, and then back to the array plane, is given by:

$$\Delta\phi_2 = 2k_0h + \underbrace{2tan^{-1}\left(\frac{f}{f_0}\right)}_{2\phi_t(f)} + \phi_{rgp}(f) \tag{4}$$

In the above, h is the height above the ground plane, k_0 the free space wavenumber, and f_0 is the cut-off frequency of layer 1 (2.3 GHz).

The middle (layer 2) and bottom/closest to the ground plane (layer 3) are FSS layers with a resistivity of (10Ω/sq). This resistive loading serves to attenuate in-band resonances. Specifically, layer 2 is designed to attenuate the resonance seen at 1.5 GHz. Further, layer 3 is designed to attenuate the resonance at 0.8 GHz. Simulated active VSWR results showing the response with and without these FSS layers are given in Fig. 8. For modeling, each layer was represented by equivalent circuits as in [48], [49]. Notably, as compared to previous works [35], [36], [39], this FSS network limits losses to a restricted bandwidth (achieving a more targeted resonance suppression).

Field distribution plots in the presence and absence of the FSS network layers are given in Fig. 9. These cross sectional

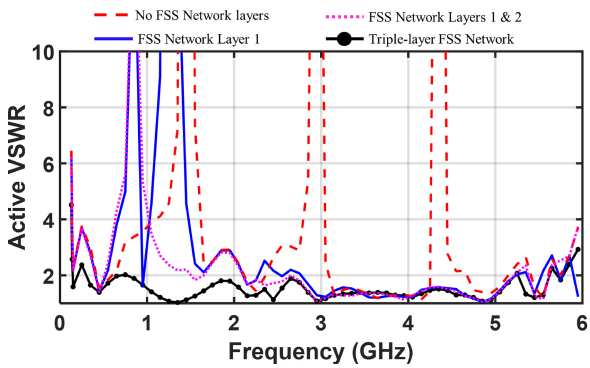

FIGURE 8. Broadside performance of the array aperture with and without FSS layers, showing suppression of resonances after FSS layer inclusion.

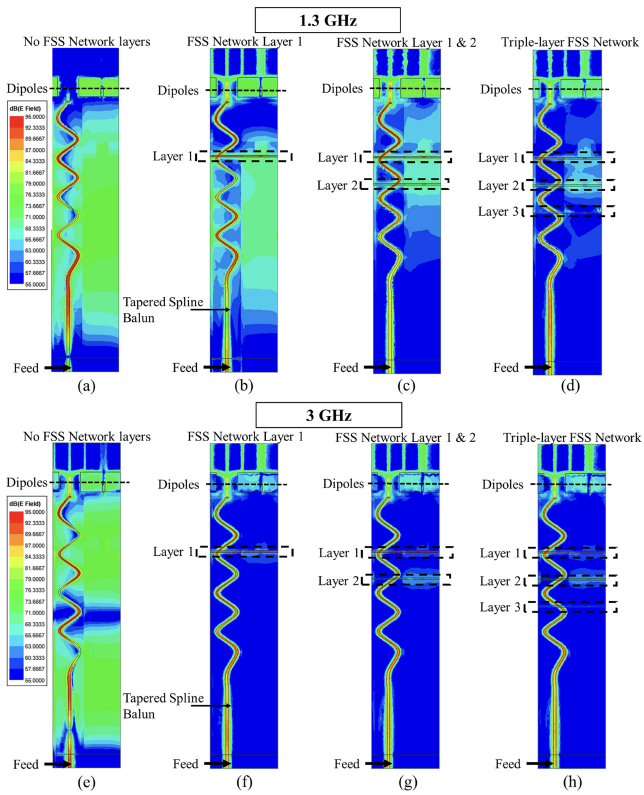

FIGURE 9. Simulated broadside E-field distribution within the array aperture substrate at selected frequencies showing the suppression of resonances after FSS layer inclusions.

field plots show the progressive suppression of resonances with the inclusions of FSS layers. Notably, FSS layer 1 is not sufficient to suppress all resonances, particularly the one seen at 1.5 GHz. The latter was only shifted to lower frequency, but remained. Adding FSS layer 2 is still not sufficient to suppress the resonance at 0.8 GHz. That is, all resonances are suppressed only after inserting the three FSS layers. It is remarked that layer 2 is responsible for suppressing the 1.3 GHz resonance as depicted in Fig. 9(c). Similarly, it is noted that layer 3 attenuates the resonance at 0.8 GHz, while not affecting antenna performance at the current frequency. Importantly, the combination of the three FSS layers serve

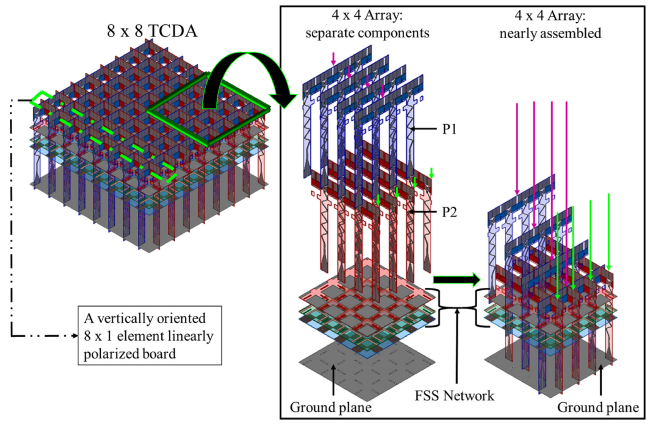

FIGURE 10. Fabricated TCDA: (a) 8 × 8 simulation model with an exploded view of the corner 4 × 4 array showing the array assembly procedure in the 'egg-create' configuration. As labeled, boards 'P1' refer to polarization 1, and boards 'P2' refer to polarization 2.

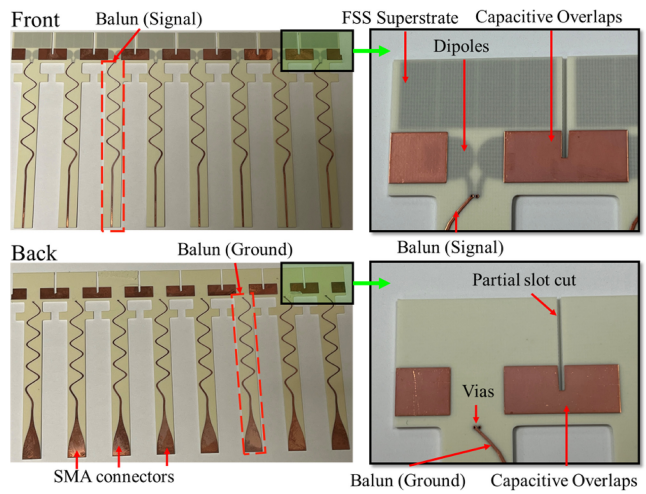

FIGURE 11. Fabricated TCDA: 8 × 1 element linearly polarized board (within polarization 2). Designing using through vias (diameter of 6 mils) decreases cost and fabrication complexity.

to suppress common-mode resonances during scanning as well.

V. FABRICATION AND ASSEMBLY

To assess the new TCDA's performance, an 8 × 8 (12 × 12 element FSS network footprint) prototype was fabricated. As depicted in Fig. 10, and Fig. 11, vertically oriented 8 × 1 element boards (comprising polarization 2), are first passed through each horizontally oriented FSS layers and the ground plane. This was done using slots that were cut through each horizontal layer to allow the feed of the vertical boards to pass through and be secured. The boards comprising polarization 1 are inserted orthogonal to the boards comprising polarization 2 to form the 'egg-crate' configuration.

The height of each FSS layer and the ground plane were adjusted appropriately and secured using nylon screws along the edge of the array. The array aperture depth below the ground plane is dependent on the space required to solder SMA connectors (in this case 5 mm). Additional copper is

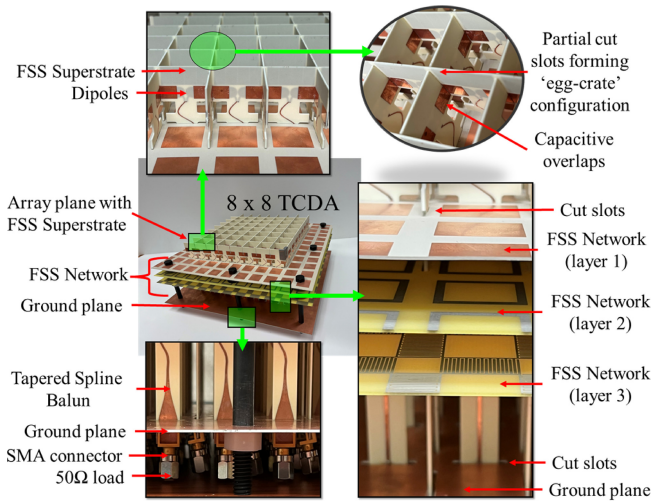

FIGURE 12. Fabricated prototype highlighting design features.

etched away around the slots cut through the ground plane to avoid shorting the baluns/connectors. The constructed array prototype is shown in Fig. 12.

VI. SIMULATION AND MEASUREMENTS

A. INFINITE ARRAY SIMULATIONS

An infinite array simulation was carried out using the periodic unit cell in Fig. 6. As seen in Fig. 13 (also Fig. 8), the presented dual-polarized TCDA shows an impressive bandwidth 40:1 and operates from 0.14 to 5.85 GHz with VSWR < 2 at broadside for nearly the entire band. Of course, and as is the case with all scanning arrays, the VSWR deteriorates with scanning [22], [39], [40], [53]. For our case, there is a single instance at 60° when the plotted (only for measurements) VSWR in Fig. 13 crosses the VSWR $= 3$ at a single frequency. Given the oddity of this spike, it can be concluded that is mismatch spike is due to the finite size of the 8×8 array. Moreover, the infinite array still maintains a VSWR < 3 when scanning in both E- and H-plane down to 60°. One possible solution to this mismatch, other than increasing the number of elements in the array, is the addition of higher order impedance matching superstrate layers. However, this leads to increased fabrication and assembly complexity and cost, as well as an increase in array thickness.

B. ACTIVE IMPEDANCE AND GAIN MEASUREMENTS

To verify performance, active VSWR and gain measurements were conducted. Specifically, the active VSWR measurements were conducted using an Agilent Technologies E5071C ENA Series Network Analyzer. Gain measurements across 190 MHz to 650 MHz were completed outdoors employing an A.H Systems Log Periodic Antenna (LPA) and an N9912A FieldFox Handheld RF Analyzer. Gain measurements from 650 MHz to 5.85 GHz were carried out in our MVG Starlab anechoic antenna chamber.

Specifically, the active VSWR was computed by adding the linear reflection coefficient of the antenna element under

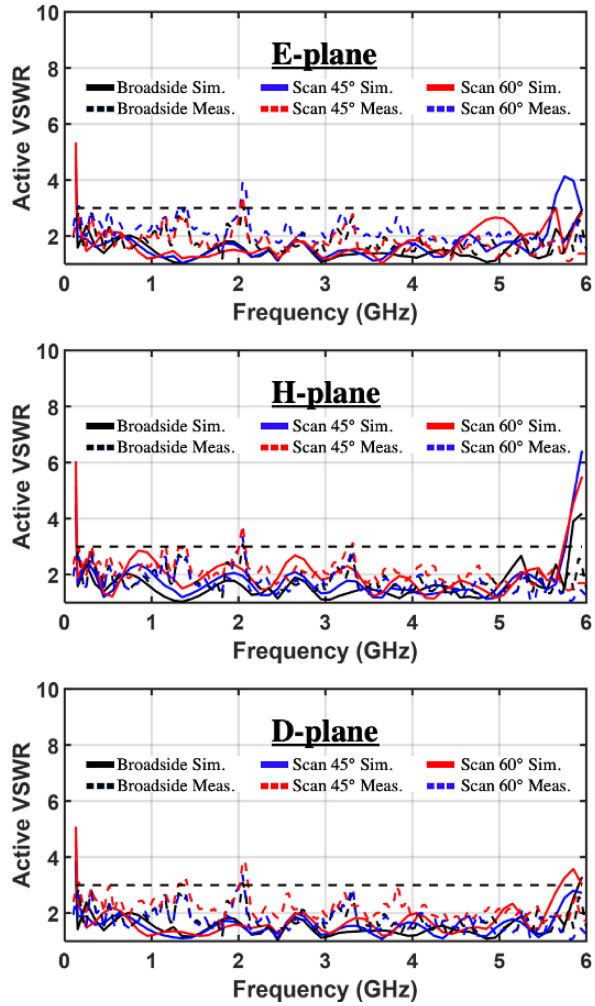

FIGURE 13. Measured vs. simulated active VSWR curves in the (top) E-, (middle) H-, and (bottom) D-planes, for $\theta = 0°$, 45°, and 60° scanning.

test along with the coupling terms from the surrounding array elements. That is, the mutual coupling from neighboring elements is combined with the return loss of the antenna elements under test, assuming uniform feeding and a square lattice. The active S-parameters of the p,q element can be found in equation (5) below:

$$\Gamma_{p,q}(\theta,\ \phi) = \sum_{m=1}^{M}\sum_{n=1}^{N} S_{mn,pq} e^{-jD([m-p]u+[n-q]v)} \tag{5}$$

Here (θ, ϕ) is the array scan direction, $u = k\sin\theta\cos\phi$ and $v = k\sin\theta\sin\phi$ are the u-v coordinates, and k is the free-space wavenumber. $S_{mn,pq}$ refers to the measured S-parameters mn for pq elements, and M, N and D are the number of elements along the x and y direction and the lattice spacing, respectively [11], [50]. Good scanning agreement is seen down to $\theta = \pm 60°$. The slight differences between the measured and simulated co-polarized gain, can be attributed to the finite size of the array. This is particularly true at the lower frequencies where the size of the array is quite small compared to the wavelength. Specifically, this effect is observed

TABLE 2. Performance trade-off comparison with previous work.

Work	Achieved Bandwidth	Average Efficiency	VSWR (0deg|60deg)	Balun	Height ($\lambda_{ref} = 140MHz$)
[35]	21:1	77% (Rad.)	$< 3 \mid < 3.5$	Twin 50Ω Coaxial Lines	$\lambda_{ref}/36.23$
[36]	13.1:1	60% (Total)	$< 2.5 \mid < 3.1$	Folded Marchand	$\lambda_{ref}/17.55$
[39]	46:1	72% (Rad.)	$< 3.1 \mid < 4$	Tapered Stripline	$\lambda_{ref}/12.18$
[40]	28:1	83% (Rad.)	$< 2.5 \mid < 3.5$	Klopfenstein Taper	$\lambda_{ref}/20.71$
[This Work]	40:1	75% (Rad.)	$< 2.5 \mid < 3.5$	Tapered Meandering Spline	$\lambda_{ref}/17.93$

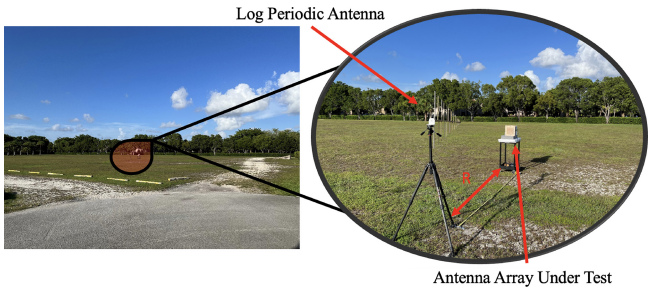

FIGURE 14. Outdoor measurement setup for 190 MHz to 650 MHz.

FIGURE 15. Testing of the fabricated TCDA prototype within our MVG Starlab anechoic antenna chamber from 650 MHz to 5.85 GHz.

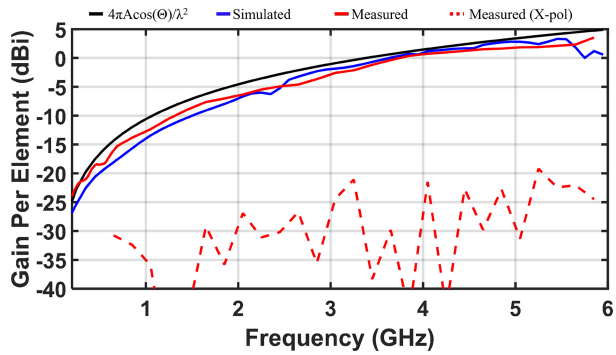

FIGURE 16. Simulated and measured (embedded) broadside gain of the developed TDCA from 190 MHz to 5.85 GHz. Cross-polarization is shown to be approximately -20 dB below the main polarization for most of the operational band. Notably, our measurements could not extend down to 140 MHz (the lowest design frequency).The authors note that higher broadside measured gain values are seen at the lowest part of the band due to ground plane reflections during outside measurements. However, the gain pattern still closely follows the simulated behaviour.

at 650 MHz where the array aperture is only λ/18. Such finite array effects are well known and documented in UWB arrays, especially tightly coupled and connected arrays, where the array emulates an infinite current sheet [39], [51].

Fig. 14 shows the outdoor measurement set-up. The LPA is placed a minimum of 1.5 meters above the ground to minimize reflections. Gain calculations were then done using the Friis transmission equation [52]. Specifically, the gain of the presented TCDA was computed from:

$$G_{TCDA} = \frac{P_R(4\pi R)^2}{P_t G_{LPA} \lambda^2} \tag{6}$$

In the above, P_r is the received power at the TCDA, and P_t refers to the transmitted power via the LPA of gain G_{LPA}. R is the distance between the TCDA and the LPA and λ is the wavelength for operation reference.

The indoor measurement set-up is depicted in Fig. 15. Fig. 16 shows the extracted broadside gain per array element while all other array elements were terminated via a 50Ω load. Fig. 17 gives the measured radiation patterns, which also closely follow simulations. As predicted, the low-frequency radiation patterns show wider beam widths because the array is only λ/18 at 650 MHz. The theoretical aperture gain $4\pi A\cos(\theta)/\lambda^2$, where A is the array element area, is also included as a reference. It is observed that the center element gain is in agreement with the simulated realized gain, including the expected drop at approximately 2.3 GHz due to the FSS network loading. A similar, but less significant drop is seen at approximately 0.8 GHz. Notably, cross-polarized radiation measures < -20 dBi over the majority of the band. It is remarked that small differences between the simulated and measured gain patterns stem from the presence of small physical misalignments in the prototype.

The overall radiation efficiency is 75% (see Fig. 18). Two efficiency lows are seen corresponding to the suppression of the resonances in the lower band. Also, at lower frequencies the efficiency is less due to the more pronounced effect of the FSS network loading. It is noted that the 0.64 mm thick FR4 boards provide structural stability and prevented any sagging in the middle of the array.

VII. CONCLUSION

This paper presented the design, fabrication, and validation (via measurements) of a bandwidth enhanced TCDA. Notably, the design employs 1) a triple-layer semi-resistive FSS network and 2) a new compact integrated meandering tapered spline balun. The trade-offs of efficiency and bandwidth of the array was discussed. A fabricated dual-polarized 8 × 8 (12 × 12 element FSS network footprint) array prototype achieves a contiguous impedance bandwidth of 140 MHz to 5.85 GHz when scanning down to ±60° (VSWR < 3.5) in the E-, H-, and D-planes. A key aspect

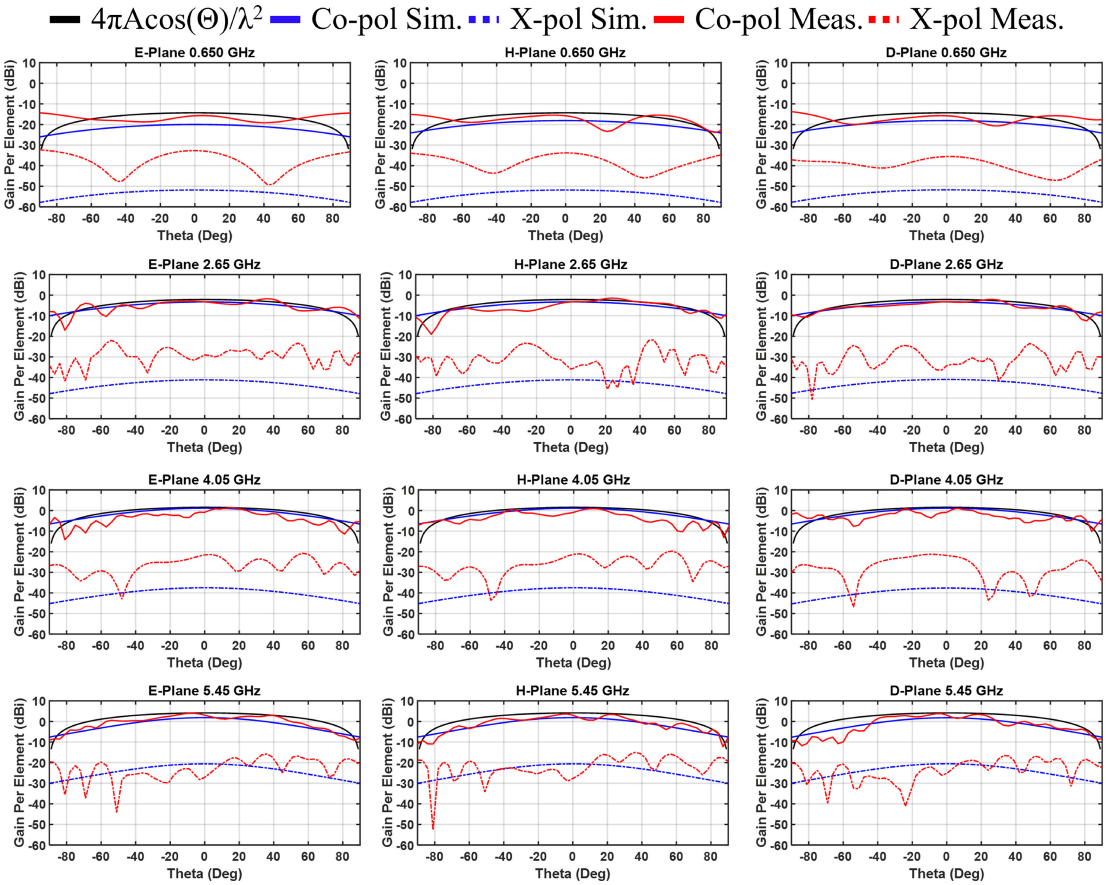

FIGURE 17. Simulated and measured radiation patterns of the proposed TCDA's center array element in E-, H-, and D-planes at 650 MHz, 2650 MHz, 4050 MHz, and 5450 MHz.

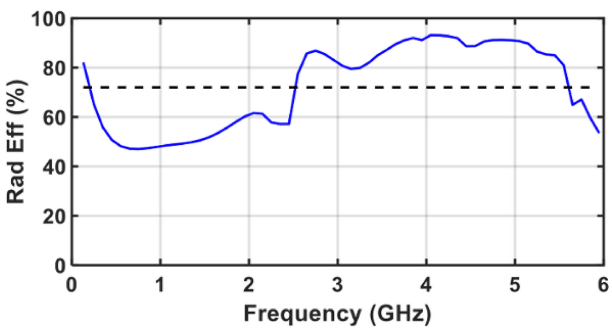

FIGURE 18. Simulated radiation efficiency of the proposed TCDA. The average across the operational bandwidth is 75%.

of the array is its low profile being $\lambda_{Low}/17.93$ (where λ_{Low} is the wavelength at the lowest frequency of operation, 140 MHz). That is, as conveyed in Table 2, compared to previous UWB TCDAs with contiguous operational bandwidths of 40:1 or greater, the proposed array is 30% thinner and has equally good or better efficiency.

ACKNOWLEDGMENT

Matthew W. Nichols would like to thank Dr. Stavros Koulouridis for his inputs in the preparation of this manuscript.

REFERENCES

[1] "National telecommunications and information administration (NTIA): United States frequency allocation chart." 2016. [Online] Available: https://www.ntia.doc.gov/page/2011/united-states-frequency-allocation-chart

[2] "Federal communications commission (FCC) auction 97 advanced wireless services (AWS-3)." 2015. [Online] Available: https://www.fcc.gov/auction/97

[3] "What is SWaP-C?" BAE Systems. 2023. [Online]. Available: https://www.baesystems.com/en-us/definition/what-is-swap-c

[4] E. de Lera Acedo, N. Razavi-Ghods, L. E. Garcia, P. Duffett-Smith, and P. Alexander, "Ultra-wideband aperture array element design for low frequency radio astronomy," *IEEE Trans. Antennas Propag.*, vol. 59, no. 6, pp. 1808–1816, Jun. 2011.

[5] D. Siafarikas, E. A. Alwan, and J. L. Volakis, "Interference mitigation for 5G millimeter-wave communications," *IEEE Access*, vol. 7, pp. 7448–7455, 2019.

[6] X. Xu and R. M. Narayanan, "FOPEN SAR imaging using UWB step-frequency and random noise waveforms," *IEEE Trans. Aerosp. Electron. Syst.*, vol. 37, no. 4, pp. 1287–1300, Oct. 2001.

[7] C.-P. Lai and R. M. Narayanan, "Ultrawideband random noise radar design for through-wall surveillance," *IEEE Trans. Aerosp. Electron. Syst.*, vol. 46, no. 4, pp. 1716–1730, Oct. 2010.

[8] N. Saputra and J. R. Long, *FM-UWB Transceivers for Autonomous Wireless Systems* (Series in Circuits and Systems). Aalborg, Denmark: River Publ., 2017.

[9] J. D. Taylor, *Introduction to Ultra-Wideband Radar Systems*. Abingdon, U.K.: Taylor and Francis, 1994.

[10] H. A. Wheeler, "Fundamental limitations of small antennas," *Proc. IRE*, vol. 35, no. 12, pp. 1479–1484, Dec. 1947.

[11] M. N. Vouvakis and D. H. Schaubert, "Vivaldi antenna arrays," in *Frontiers in Antennas*. New York, NY, USA: McGraw-Hill Prof., 2011, ch. 3, pp. 127–168.

[12] J. T. Logan, R. W. Kindt, and M. N. Vouvakis, "Low cross-polarization Vivaldi arrays," *IEEE Trans. Antennas Propag.*, vol. 66, no. 4, pp. 1827–1837, Apr. 2018.

[13] A. Elsherbini et al., "UWB antipodal Vivaldi antennas with protruded dielectric rods for higher gain, symmetric patterns and minimal phase center variations," in *Proc. IEEE Antennas Propag. Soc. Int. Symp.*, 2007, pp. 1973–1976.

[14] J. T. Logan, R. W. Kindt, and M. N. Vouvakis, "A 1.2-12 GHz sliced notch antenna array," *IEEE Trans. Antennas Propag.*, vol. 66, no. 4, pp. 1818–1826, Apr. 2018.

[15] M. W. Elsallal and J. C. Mather, "An ultra-thin, decade (10: 1) bandwidth, modular 'BAVA' array with low cross-polarization," in *Proc. IEEE Int. Symp. Antennas Propag. (APSURSI)*, 2011, pp. 1980–1983.

[16] J. T. Logan, R. W. Kindt, M. Y. Lee, and M. N. Vouvakis, "A new class of planar ultrawideband modular antenna arrays with improved bandwidth," *IEEE Trans. Antennas Propag.*, vol. 66, no. 2, pp. 692–701, Feb. 2018.

[17] S. Applebaum, "Adaptive arrays," *IEEE Trans. Antennas Propag.*, vol. 24, no. 5, pp. 585–598, Sep. 1976.

[18] H. Holter, "Dual-polarized broadband array antenna with BOR-elements, mechanical design and measurements," *IEEE Trans. Antennas Propag.*, vol. 55, no. 2, pp. 305–312, Feb. 2007.

[19] H. Steyskal, "Digital beamforming antennas: An introduction," *Microw. J.*, vol. 30, no. 1, Jan. 1987, Art. no. 107124.

[20] J. A. Kasemodel, C.-C. Chen, and J. L. Volakis, "Low-cost, planar and wideband phased array with integrated balun and matching network for wide-angle scanning," in *Proc. IEEE Antennas Propag. Soc. Int. Symp.*, 2010, pp. 1–4.

[21] M. H. Novak and J. L. Volakis, "Ultra-wideband phased arrays," in *Antenna Engineering Handbook*, 5th ed., J. L. Volakis, Ed. New York, NY, USA: McGraw-Hill, ch. 30, 2019.

[22] H. Wheeler, "Simple relations derived from a phased-array antenna made of an infinite current sheet," *IEEE Trans. Antennas Propag.*, vol. 13, no. 4, pp. 506–514, Jul. 1965.

[23] B. Tomasic and H. Steyskal, "Minimum Q of the element in an infinite phased array," in *Proc. IEEE Antennas Propag. Soc. Int. Symp.*, 2007, pp. 145–148.

[24] B. Tomasic and H. Steyskal, "Minimum Q of the element in an infinite phased array—TMz case," in *Proc. 19th Int. Conf. Appl. Electromagn. Commun.*, Sep. 2007, pp. 1–8.

[25] J. P. Doane, K. Sertel, and J. L. Volakis, "Bandwidth limits for lossless planar arrays over ground plane," *Electron. Lett.*, vol. 48, no. 10, pp. 540–542, May 2012.

[26] J. P. Doane, K. Sertel, and J. L. Volakis, "Matching bandwidth limits for arrays backed by a conducting ground plane," *IEEE Trans. Antennas Propag.*, vol. 61, no. 5, pp. 2511–2518, May 2013.

[27] J. P. Doane, K. Sertel, and J. L. Volakis, "Bandwidth limits for lossless, reciprocal PEC-backed arrays of arbitrary polarization," *IEEE Trans. Antennas Propag.*, vol. 62, no. 5, pp. 2531–2542, May 2014.

[28] B. A. Munk, "Broadband wire arrays," *Infinite Antenna Arrays and FSS*. Hoboken, NJ, USA: Wiley-IEEE Press, 2003, pp. 181–213.

[29] J. P. Doane, K. Sertel, and J. L. Volakis, "A wideband, wide scanning tightly coupled dipole array with integrated balun (TCDA-IB)," *IEEE Trans. Antennas Propag.*, vol. 61, no. 9, pp. 4538–4548, Sep. 2013.

[30] J. Zhong, A. Johnson, E. A. Alwan, and J. L. Volakis, "Dual-linear polarized phased array with 9:1 Bandwidth and 60° scanning off broadside," *IEEE Trans. Antennas Propag.*, vol. 67, no. 3, pp. 1996–2001, Mar. 2019.

[31] H. Zhang, S. Yang, S. Xiao, Y. Chen, and S. Qu, "Low-profile, lightweight, ultra-wideband tightly coupled dipole arrays loaded with split rings," *IEEE Trans. Antennas Propag.*, vol. 67, no. 6, pp. 4257–4262, Jun. 2019.

[32] E. Yetisir, N. Ghalichechian, and J. L. Volakis, "Ultrawideband array with 70° scanning using FSS superstrate," *IEEE Trans. Antennas Propag.*, vol. 64, no. 10, pp. 4256–4265, Oct. 2016.

[33] A. O. Bah, P.-Y. Qin, R. W. Ziolkowski, Q. Cheng, and Y. J. Guo, "Realization of an ultra-thin metasurface to facilitate wide bandwidth wide angle beam scanning," *Sci. Rep.*, vol. 8, p. 4761, Mar. 2018.

[34] Y. E. Erdemli, K. Sertel, R. A. Gilbert, D. E. Wright, and J. L. Volakis, "Frequency-selective surfaces to enhance performance of broad-band reconfigurable arrays," *IEEE Trans. Antennas Propag.*, vol. 50, no. 12, pp. 1716–1724, Dec. 2002.

[35] W. F. Moulder, K. Sertel, and J. L. Volakis, "Superstrate-enhanced ultrawideband tightly coupled array with resistive FSS," *IEEE Trans. Antennas Propag.*, vol. 60, no. 9, pp. 4166–4172, Sep. 2012.

[36] D. K. Papantonis and J. L. Volakis, "Dual-polarized tightly coupled array with substrate loading," *IEEE Antennas Wireless Propag. Lett.*, vol. 15, pp. 325–328, 2016.

[37] N. J. Smith, D. Papantonis, and J. L. Volakis, "Bandwidth reconfigurable metamaterial arrays," *Int. J. Antennas Propag.*, vol. 2014, Jun. 2014, Art. no. 397576. [Online]. Available: https://doi.org/10.1155/2014/397576

[38] Z. Szabó, G.-H. Park, R. Hedge, and E.-P. Li, "A unique extraction of metamaterial parameters based on Kramers-Kronig relationship," *IEEE Trans. Microw. Theory Techn.*, vol. 58, no. 10, pp. 2646–2653, Oct. 2010.

[39] A. D. Johnson, J. Zhong, S. B. Venkatakrishnan, E. A. Alwan, and J. L. Volakis, "Phased array with low-angle scanning and 46:1 Bandwidth," *IEEE Trans. Antennas Propag.*, vol. 68, no. 12, pp. 7833–7841, Dec. 2020.

[40] M. Carvalho, A. D. Johnson, E. A. Alwan, and J. L. Volakis, "Semi-resistive approach for tightly coupled dipole array bandwidth enhancement," *IEEE Open J. Antennas Propag.*, vol. 2, pp. 110–117, 2021.

[41] M. Carvalho, A. D. Johnson, E. A. Alwan, and J. L. Volakis, "Frequency selective surface network for in-phase ground plane reflections in tightly coupled dipole arrays," in *Proc. Int. Appl. Comput. Electromagn. Soc. Symp. (ACES)*, 2020, pp. 1–2.

[42] D. M. Pozar, *Microwave Engineering*. Hoboken, NJ, USA: Wiley, 2005, ch. 5, pp. 258–261.

[43] R. W. Klopfenstein, "A transmission line taper of improved design," *Proc. IRE*, vol. 44, no. 1, pp. 31–35, Jan. 1956.

[44] C. Li and C. Zhu, "Designing developable C-Bézier surface with shape parameters," *Mathematics*, vol. 8, no. 3, p. 402, Mar. 2020. [Online]. Available: http://dx.doi.org/10.3390/math8030402

[45] A. O. Bah, P.-Y. Qin, R. W. Ziolkowski, Y. J. Guo, and T. S. Bird, "A wideband low-profile tightly coupled antenna array with a very high figure of merit," *IEEE Trans. Antennas Propag.*, vol. 67, no. 4, pp. 2332–2343, Apr. 2019.

[46] Y. Ma, F. Pollick, and W. T. Hewitt, "Using B-spline curves for hand recognition," in *Proc. 17th Int. Conf. Pattern Recognit. (ICPR)*, vol. 3, 2004, pp. 274–277.

[47] H. Pottmann, S. Leopoldseder, and M. Hofer, "Approximation with active b-spline curves and surfaces," in *Proc. 10th Pacific Conf. Comput. Graph. Appl.*, 2002, pp. 8–25.

[48] S. M. A. M. H. Abadi and N. Behdad, "Design of wideband, FSS-based multibeam antennas using the effective medium approach," *IEEE Trans. Antennas Propag.*, vol. 62, no. 11, pp. 5557–5564, Nov. 2014.

[49] Y. Xu and M. He, "Design of multilayer frequency-selective surfaces by equivalent circuit method and basic building blocks," *Int. J. Antennas Propag.*, vol. 2019, Aug. 2019, Art. no. 9582564. [Online]. Available: https://doi.org/10.1155/2019/9582564

[50] N. Amitay, V. Galindo, and C. P. Wu, *Theory and Analysis of Phased Array Antennas*. Nashville, TN, USA: Wiley, 1972.

[51] I. Tzanidis, K. Sertel, and J. L. Volakis, "UWB low-profile tightly coupled dipole array with integrated balun and edge terminations," *IEEE Trans. Antennas Propag.*, vol. 61, no. 6, pp. 3017–3025, Jun. 2013.

[52] C. A. Balanis, *Antenna Theory: Analysis and Design*, 4th ed. Hoboken, NJ, USA: Wiley, 2005.

[53] M. R. Islam, M. Carvalho, S. B. Venkatakrishnan, and J. L. Volakis, "Packable and readily deployable tightly coupled dipole array (TCDA) with integrated planar balun," *IEEE Open J. Antennas Propag.*, vol. 2, pp. 110–117, 2022.

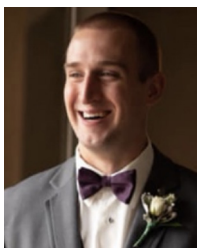

MATTHEW W. NICHOLS (Member, IEEE) received the B.S. degree in electrical engineering from Western New England University, Springfield, MA, USA, in 2018, and the M.S. degree in electrical and computer engineering from Florida International University, Miami, FL, USA, in 2021, where he is currently pursuing the Ph.D. degree with RFCOM Lab. His research interests include deployable array apertures, textile electronics, wideband array apertures, and mm-wave phased arrays. He was a recipient of the NASA Research Announcement Fellowship Award in 2019.

MICHAIL O. ANASTASIADIS (Graduate Student Member, IEEE) received the B.S. degree in electrical and computer engineering and the M.S. degree in telecommunication systems from the Democritus University of Thrace, Xanthi, Greece, in 2017 and 2019, respectively. He is currently pursuing the Ph.D. degree with Florida International University, Miami, FL, USA. His research interests include plasma-wave devices and vacuum electronics.

MALCOLM E. TAAFFE (Member, IEEE) received the B.S. degree in electrical engineering from Florida International University, Miami, FL, USA, in 2020, where he has been working with RFCOM Lab since 2019.

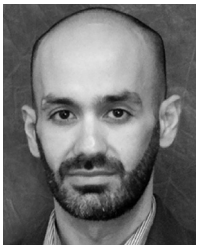

ELIAS A. ALWAN (Member, IEEE) was born in Aitou, Lebanon, in 1984. He received the B.E. degree (summa cum laude) in computer and communication engineering from Notre Dame University-Louaize, Zouk Mosbeh, Lebanon, in 2007, the M.E. degree in electrical engineering from the American University of Beirut, Beirut, Lebanon, in 2009, and the Ph.D. degree in electrical and computer engineering from The Ohio State University (OSU), Columbus, OH, USA, in 2014. He is currently an Eminent Scholar Chaired Assistant Professor with the Department of Electrical and Computer Engineering, Florida International University, Miami, FL, USA. From 2015 to 2017, he was a Senior Research Associate with the Electro Science Laboratory, OSU. His research interests include antennas and radio frequency systems with particular focus on ultra-wideband communication systems, including UWB arrays, reduced hardware and power-efficient communication back-ends, and millimeter-wave technologies for 5G applications. He was the recipient of the 2020 NSF CAREER Award. He has been a Phi Kappa Phi Member since 2010.

JOHN L. VOLAKIS (Life Fellow, IEEE) was born in Chios, Greece, in 1956, and immigrated to USA, in 1973. He received the B.E. degree (summa cum laude) from Youngstown State University, Youngstown, OH, USA, in 1978, and the M.Sc. and Ph.D. degrees from The Ohio State University, Columbus, OH, USA, in 1979 and 1982, respectively.

He started his career with Rockwell International North American Aircraft Operations from 1982 to 1984, and currently with Boeing. In 1984, he was appointed an Assistant Professor with the University of Michigan, Ann Arbor, MI, USA, and became a Full Professor in 1994. He also served as the Director of Radiation Laboratory from 1998 to 2000. From January 2003 to August 2017, he was the Roy and Lois Chope Chair Professor of Engineering with The Ohio State University, Columbus, and served as the Director of ElectroScience Laboratory from 2003 to 2016. Since August 2017, he has been the Dean of the College of Engineering and Computing and a Professor of Electrical and Computer Engineering with Florida International University. His publications include nine books, over 450 journal papers and 950 conference papers, 33 book chapters and 32 patents/disclosures. Among his coauthored books are: *Approximate Boundary Conditions in Electromagnetics* in 1995; *Finite Element Methods for Electromagnetics* in 1998; *Antenna Engineering Handbook*, (Fourth Edition, 2007 and Fifth Edition, 2019); *Small Antennas* in 2010; *Integral Equation Methods for Electromagnetics* in 2011; and *Wearable Antennas and Electronics* (Artech House, 2022). He has graduated/mentored over 100 doctoral students/post-docs with 43 of them receiving best paper awards at conferences. Over the years, he carried out research in computational methods, antennas, wireless communications and propagation, electromagnetic compatibility and interference, design optimization, RF materials, multi-physics engineering, millimeter waves, terahertz, and medical sensing.

Prof. Volakis was the recipient of the University of Michigan College of Engineering Research Excellence Award in 1993, the Scott Award from The Ohio State University College of Engineering for Outstanding Academic Achievement in 2011, the IEEE AP Society C-T. Tai Teaching Excellence Award in 2011, the IEEE Henning Mentoring Award in 2013, the IEEE Antennas and Propagation Distinguished Achievement Award in 2014, The Ohio State University Distinguished Scholar Award in 2016, and The Ohio State University ElectroScience Laboratory George Sinclair Award in 2017, the URSI Booker Gold Medal in 2020, an Advanced Computational Electromagnetics Society Fellow, the American Association for the Advancement of Science Fellow, and the National Academy of Inventors Fellow in 2021. His service to Professional Societies include: The President of the IEEE Antennas and Propagation Society in 2004, the Chair of USNC/URSI Commission B from 2015 to 2017, twice the General Chair of the IEEE Antennas and Propagation Symposium, an IEEE APS Distinguished Lecturer, an IEEE APS Fellows Committee Chair, an IEEE-Wide Fellows Committee Member, and an Associate Editor of several journals. He was listed by ISI among the top 250 most referenced authors in 2004.